Meteorol. Z. (Contrib. Atm. Sci.), PrePub DOI 10.1127/metz/2020/1008

Energy Meteorology

Satellite image-based generation of high frequency solar radiation time series for the assessment of solar energy systems

Sebastian Schreck[1], Marion Schroedter-Homscheidt[2*], Martin Klein[1] and Karl Kiên Cao[3]

[1]Former affiliation: German Aerospace Center (DLR), Institute of Engineering Thermodynamics, Stuttgart, Germany
[2]German Aerospace Center (DLR), Institute of Networked Energy Systems, Oldenburg, Germany
[3]German Aerospace Center (DLR), Institute of Engineering Thermodynamics, Stuttgart, Germany

(Manuscript received November 26, 2019; in revised form March 14, 2020; accepted March 16, 2020)

Abstract

Solar energy is envisaged as a major pillar of the global transition to a climate-friendly energy system. Variability of solar radiation requires additional balancing measures to ensure a stable and secure energy supply. In order to analyze this issue in detail, solar radiation time series data of appropriate temporal and spatial resolution is necessary. Common weather models and satellites are only delivering solar surface irradiance with temporal resolutions of up to 15 min. Significant short-term variability in irradiances within seconds to minutes however is induced by clouds. Ground-based measurements typically used to capture this variability are costly and only sparsely available. Hence, a method to synthetically generate time series from currently available satellite imagery is of value for researchers, grid operators, and project developers. There are efforts to increase satellite resolution to 1 min, but this is not planned everywhere and will not change the spatial resolution. Therefore, the fundamental question remains if there are alternative strategies to obtain high temporal resolution observations at a pinpoint. This paper presents a method to generate 1 min resolved synthetic time series of global and direct normal irradiances for arbitrary locations. A neural network based on satellite image derived cloud structure parameters enables to classify high-frequency solar radiation variability. Combined with clear-sky radiation data, 1 min time series which reflect the typical variability characteristics of a site are reproduced. Testing and validation against ground observations (BSRN) show that the method can accurately reproduce characteristics such as frequency and ramp distributions. An application case demonstrates the usage in low-voltage grid studies.

Keywords: Solar radiation variability, 1 min time series, neural networks, synthetic time series, distribution grid, voltage violations

1 Introduction

The envisaged shift to a renewable energy-based energy system as well as the ever-decreasing costs for solar based renewable energy technologies like photovoltaics (PV) leads to a surge of installed capacities. The natural volatility of solar radiation brings new challenges to the operation and planning of the power systems as additional balancing measures are required. Short-term variability in Global Horizontal Irradiance (GHI) and Direct Normal Irradiance (DNI) induces strong ramps in power systems dominated by PV and increases grid integration challenges (e.g. as described in Wiemken et al., 2001; Lave and Kleissl, 2010; Jamaly et al., 2013; Lave et al., 2015). To study the impact of the increasing variable power infeed, energy system models with various temporal and spatial foci are used.

The impact of the temporal modelling resolution on the model results is frequently discussed in the literature. These models can range from small household PV-battery systems to trans-regional energy system models. Using input-data with inappropriate (i.e. too low) temporal resolution might lead to an underestimation of necessary ramp-rates of conventional power power plants, storage cycles (Deane et al., 2014), or an overestimation of self-consumption capabilites (Wolf and Vèelák, 2018).

Short-term fluctuations of solar radiation at a range of seconds to minutes are mainly induced by moving clouds and can hence be considererd a local scale phenomenon. Several studies have shown that these fluctuations are significantly smoothed out over distances (e.g. Lingfors, 2015; Perez et al., 2016). Perez et al. (2012) analyze the correlation of measurement data for two measurement sites and a variation of the distance of the sites and temporal resolution of the measurements. They show that measurements at two sites are becoming almost uncorrelated for temporal resolution-distances tuples of (1 min and 1 km, 5 min and 4 km, 15 min and 10 km).

*Corresponding author: Marion Schroedter-Homscheidt, German Aerospace Center (DLR), Institute of Networked Energy Systems, Carl-von-Ossietzky-Str. 15, 26129 Oldenburg, Germany, e-mail: marion.schroedter-homscheidt@dlr.de

Geostationary meteorological satellites in combination with clear-sky radiation models already provide solar radiation timeseries for GHI and DNI with a temporal resolution of up to 15 min with an almost global coverage (e.g. the summary chapter 4 in Sengupta et al., 2015). This is sufficient for many solar energy applications due to the spatial and temporal smoothing effects. However, temporal resolution of 1 min are discussed as being necessary for low voltage grid studies with their large spatial resolution or stand-alone systems. Such time series are nowadays only available through costly ground-based measurements which are not available everywhere. Furthermore, such observations systems do not provide historical time series of the last 10 years at a location of interest and waiting for the generation of a long-term ground-based observation is often practically not possible as such a waiting period would block the investment.

This motivates the development of methods to synthetically generate high-frequency time series at arbitrary locations. This data would be helpful for various stakeholders like grid operators, project developers, technology developers, or researchers if no or only poor ground-based measurements are available. Several approaches on the synthetic generation of these time series have been published recently. Typically, these methods rely on the combination of ground-based measurements to cluster and classify short-term variability characteristics with satellite observations and/or probabilistic methods:

Fernández-Peruchena and Gastón (2016) propose a method to increase the temporal resolution of GHI of hourly resolved satellite data to 1 min. Using the clearsky-index distribution of minute-wise ground-based measurements of a site, their method matches the closest day in terms of euclidean distance of that site to the satallite data. They achieve low Root Mean Square Errors (RMSE) in a range of 1.7 %–8 %. However, the approach is not applicable to arbitrary locations as it relies on existing measurement data being available at the same location already. Grantham et al. (2017) desribe a method to generate value pairs of GHI and DNI at a temporal resolution of 5 min from hourly resolved observations. Their method applies a classification approach of the atmospheric condition by separating into clear sky classes. Li et al. (2017) use ground-based measurements of four different climatic zones in the United States to cluster different variablity classes. Subsequently, they use a Markov Chain model to account for the transition propablities between variability classes. They show that 3 min timeseries of GHI can be reproduced for the four different zones analyzed.

Jung (2015) and as a follow-on Schroedter-Homscheidt et al. (2018) introduced variability classes relying on both the clear sky index (k_c) properties and the frequency and amplitude of ramping irradiances. The ramping characteristics are described with various variability indices as well as by upper and lower envelope curves and the width between them. This classification was used e.g. by Nouri et al. (2019) for the uncertainty specification of all sky imager irradiance nowcasts.

In this paper, satellite-based cloud structural parameters are used to derive an automatic, neural network based detection of the variability classes from satellite-based observations only. The variability classification and the underlying reference database are then used to generate artificial 1 min time series with the same statistical properties as a 1 min local observation would have shown.

In Section 2 of this paper, the data basis and data preprocessing for the neural network classification is presented. Section 3 describes the process of generating the synthetic time series and introduces metrics to benchmark the synthetic time series to ground based measurements. Additionally, an application case of the synthetic radiation data for a low-voltage grid study is presented. The results of the benchmark as well as the application case are illustrated in Section 4. Section 5 concludes the results and discusses possible enhancements of the approach.

2 Data basis

2.1 Ground-based measurements

Ground-based measurements for the training, testing and validation of the model are obtained from four BSRN (Ohmura et al., 1998) stations across Europe (Fig. 1, Table 1). Records of yearly DNI and GHI time series at 1 min resolutions are used. The stations are chosen to cover different solar radiation conditions, climates as well as distinguishable distributions of variability and variability classes as described in Schroedter-Homscheidt et al. (2018).

The 1 min measurement data is used for both model calibration and validation purposes. For model training and testing an hourly variability classification is derived as described in Schroedter-Homscheidt et al. (2018). Eight variability classes are distinguished from clear to overcast cloudy conditions with decreasing k_c and low, medium, or high temporal direct normal radiation 1 min variability. Examples of the variability classes as well as statistical characteristics can be found in Annex A1. The selection is made on the basis of various variability indices as well as upper and lower envelopes of the timeseries. Schroedter-Homscheidt et al. (2018) provides a detailed description of statistical characteristics of the eight variability classes with respect to variability indices of global and direct irradiance. A total number of 29 290 hours over 9 observation years is classified.

For validation purposes, the measurement data is used to benchmark the synthetically generated DNI and GHI timeseries. The applied dataset split and evaluation metrics are described in Section 3.

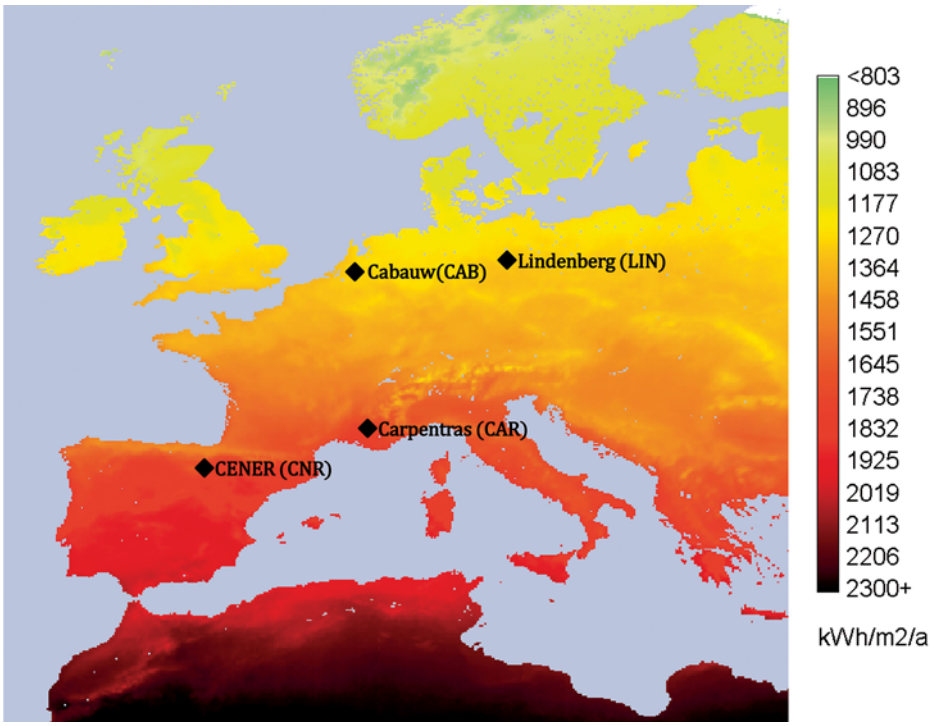

Figure 1: BSRN stations used for model calibration and validation on a heat map of yearly GHI – adapted from (Scholz, 2012).

Table 1: Overview of BSRN stations and datasets used.

Station ID	Station name	Country	Lat [°]	Lon [°]	Altitude [m]	Years	Application
CAR	Carpentras	France	44.083	5.059	100	2006,2012	Calibration
CAB	Cabauw	Netherlands	51.971	4.926	0	2010–2012	Calibration
CNR	Cener	Spain	42.816	−1.601	471	2010–2012	Calibration
LIN	Lindenberg	Germany	52.210	14.122	125	2006	Validation

2.2 APOLLO cloud parameters

For the same observation years as described in Table 1, cloud properties are derived from multi-spectral observations of the Meteosat Second Generation (MSG) satellites. MSG's Spinning Enhanced Visible and InfraRed Imager (SEVIRI) covers Africa, continental Europe, and the South of Scandinavia in 15 min scanning intervals and a spatial resolution of approx. 4×5 km^2 to 5×6 km^2 in Europe. For all obervation years together this yields a total of 98 938 cloud parameter sets in 15 min temporal resolution.

The APOLLO (AVHRR Processing scheme Over cLouds Land and Ocean, originally developed for the AVHRR instrument, Kriebel et al., 1989; Saunders and Kriebel, 1988; Kriebel et al., 2003) methodology delivers cloud mask and cloud physical parameters for all satellite pixels during daytime since 1st February 2004. The pixel-wise cloud parameters include the cloud coverage given as percentage inside the pixel, the cloud type which discriminates between low-level, medium-level, and high-level reaching water or mixed-phase clouds and high-level thin ice clouds, and the cloud optical depth. Cloud coverage (i.e., the fraction inside a pixel covered by a cloud) expressed in percent, is derived for each level and the optically thin class separately. The cloud type is discriminated with the help of the cloud top temperature and a comparison against standard vertical temperature profiles. For partially cloudy pixels, a cloud type is assigned as the most frequent cloud type in a 50×50 pixel environment. Cloud optical depth (COD) is derived first only for fully cloudy pixels. The estimated optical depth of the partly covered pixel is computed by taking the COD average of all fully covered pixels of same the type of cloud in this region, and then by multiplying this average by the cloud coverage.

Additionally, textural features in a 29×29 pixel window are used. Cloud fraction in the window is derived from the ratio of all pixels being detected as cloudy and all pixels existing in the window. The number of clouds is obtained as well as the number of cloud/cloud free changes among pixels in the binary cloud mask. The fractal box dimension is used as an additional classifier representing the fractal characteristic of the cloud field (Carvalho et al., 1998).

For a detailed description of the parameters please refer to Wey and Schroedter-Homscheidt (2014), Jung (2015), and Schroedter-Homscheidt et al. (accepted).

2.3 Clear-sky radiation

An estimate of clear-sky radiation is required for both the classification of hourly variability classes and the synthetic time series generation. This data is obtained at 1 min resolution for all considered sites using the clear-sky model CAMS McClear (Lefèvre et al., 2013; Gschwind et al., 2019).

3 Methodology

This section presents a novel method for the generation of 1 min time series of DNI and GHI for arbitrary locations based on clear-sky radiation data and satellite-based textural parameters describing cloud spatial properties. Cloud patterns are identified automatically to classify the actual meteorological situation. Based on a pre-classified reference database (Schroedter-Homscheidt et al., 2018), a statistically representative 1 min resolved time series is selected and super-imposed to the clear-sky radiation time series. First, the concept is outlined followed by a detailed description of the process steps. A demonstration case for the application of the synthetic time series is subsequently presented in Section 3.2.

The full process of time series generation for one day and location is illustrated in Fig. 2. In a first step, all hours of the day between sunrise and sunset are assigned to a variability class. For each hour, four datasets of the 15 min resolved spatial cloud parameters are used as input data for a trained neural network classifier which assigns the parameters to one of the eight variability classes (step 1). Subsequently, for each classified hour a 1 min variability sample of the respective variability class is randomly drawn from a variability class database (published as a supplement in Schroedter-Homscheidt et al., 2018). This sample incorporates the dimensionless information of cloud movement induced variability in the form of a clear-sky index time series at 1 min temporal resolution (step 2a). The value of the clear-sky index k_c is defined as the ratio of the actual irradiance over a certain time period and location to the expected irradiance under clear-sky conditions. A simple multiplication of the clear sky irradiance for that day and location and the 1 min clear-sky index time series results in a synthetic 1 min profile of the specified day and location (step 2b). This approach is applicable for both DNI and GHI time series as the reference database includes both k_c samples.

3.1 Neural network classification

Artificial Neural Networks (ANN) can be used as a method for statistical classification, i.e. the assignment of an unknown observation or data sample to a specified category. In order to accurately model complex nonlinear relationships between input data (features) and the corresponding output (label) ANN require lots of training data. Satellite-based cloud parameters as described above act as features and their corresponding variability classes from a pre-classified ground-based time-series act as pre-defined labels in the training data set (Schroedter-Homscheidt et al., 2018). The satellite-based cloud parameters are used as input for a multilayer feed forward neural network which assigns a probability to each of the eight variability classes as output (step 1). An example of such a neural network with two hidden layers is presented in Fig. 3.

The input layer receives 20 cloud parameters for each 15 min of an hour, so 80 parameters for the classification of 1 h in total. As most of the input parameters have different value ranges, they are first normalized to a value range between 0 and 1. This leads to an improvement of the training process as the convergence to local minima can be increased. Since the ANN only allows numeric inputs, category parameters (e.g. the cloud area type which can either be scattered, broken overcast, clear, etc.) are transformed to binary parameters. A full list of the used APOLLO cloud parameters can be found in the Appendix (Annex A2, Table A.3).

The cross-entropy function is used as a state of the art loss function for ANN classification problems (Zhang, 2000). The output layer is defined as a softmax function yielding a classification probability for each class among a set of classes C and output values $(y_i, \ldots, y_C)$ as:

$$P(c_i) = \frac{e^{y_i}}{\sum_{k=1}^{C} e^{y_k}}, \ \forall i \in C. \tag{3.1}$$

The classified hour for a specific output of the ANN can either be chosen as the class with the highest probability among $P(c_i)$ or a weighted random choice can be applied to the output of the ANN. The results presented in Section 4 are produced using a weighted random choice since the probability distribution of the output of the ANN is relatively flat for most variability classes. This approach avoids an overrepresentation of classes with just a slightly higher probability being picked over classes with indistinctive features.

Each set of input parameters in the training dataset is then assigned to a corresponding variability class as a label. In order to avoid an overfitting of the model (i.e. that the model is only capable of accurately predicating the accuracy of the used training data, but incapable of predicting unknown data), the main part of the labeled dataset is split into a training, a validation, and a testing dataset (Fig. 4).

The validation dataset is used during the training process to benchmark various Neural Network set-ups with different hyper-parameters (Table 2). This is done to find the best performing neural network in terms of accuracy varying the number of hidden layers, neurons per layer, learning rate as well as the type of activation function and optimization algorithm used. The trained ANN model which achieves the highest validation accuracy in the validation data subset uses 2 hidden layers, 100 neu-

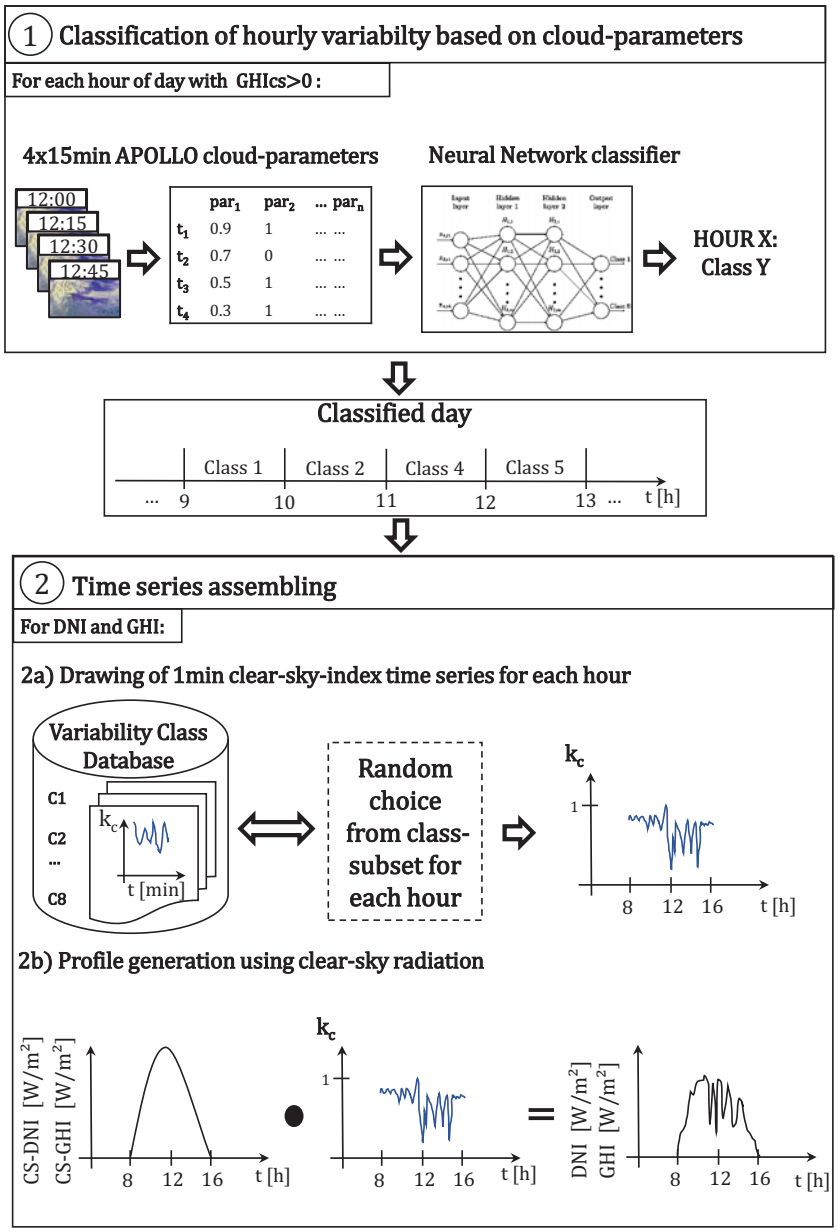

Figure 2: Schematic process overview of the method.

Table 2: Parameter ranges of hyperparameters used for ANN training.

Hyperparameter	Parameter range
Number of hidden layers	1, 2, 3
Neurons per layer	50, 100, 500, 1000
Learning rate	0.01, 0.001, 0.0001
Activation function	Sigmoid, ReLU
Optimization algorithm	Gradient-descent, ADAM

rons per layer, and a learning rate of 0.001. A detailed description and evaluation of this process is described in Schreck (2018).

The remaining dataset is kept aside for the unbiased testing of the final ANN with this optimized hyperparameter configuration.

3.2 Time series assembly

After the determination of the variability classes for each daytime hour through the ANN, the 1 min time series are assembled in an hourly piece-wise manner. In this section, this process is demonstrated for DNI and a day with mixed cloud conditions, i.e. cloud free at mid-day and cloudy morning and evening situations. The same procedure is also applicable to GHI time series as later shown in the results section.

In this step 2a, for each hour a sample of k_c values is randomly drawn from the clear-sky index reference database subset corresponding to the derived variability class for this hour. This leads to a time series with 1 min resolution of k_c values for the respective day (Fig. 5a). The shown example illustrates that there is nearly no

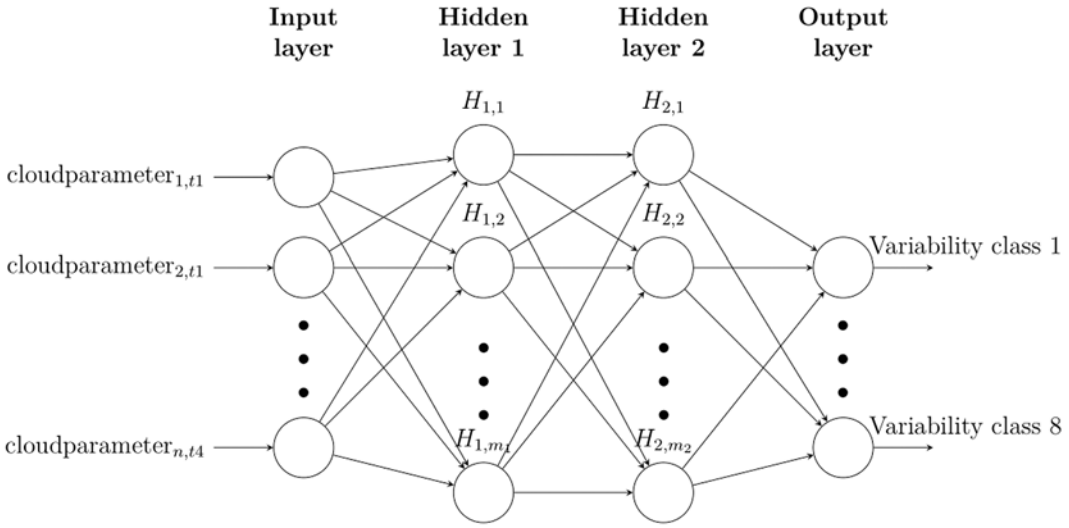

Figure 3: Structure of a multilayer feed forward ANN designed as a multiclass classifier.

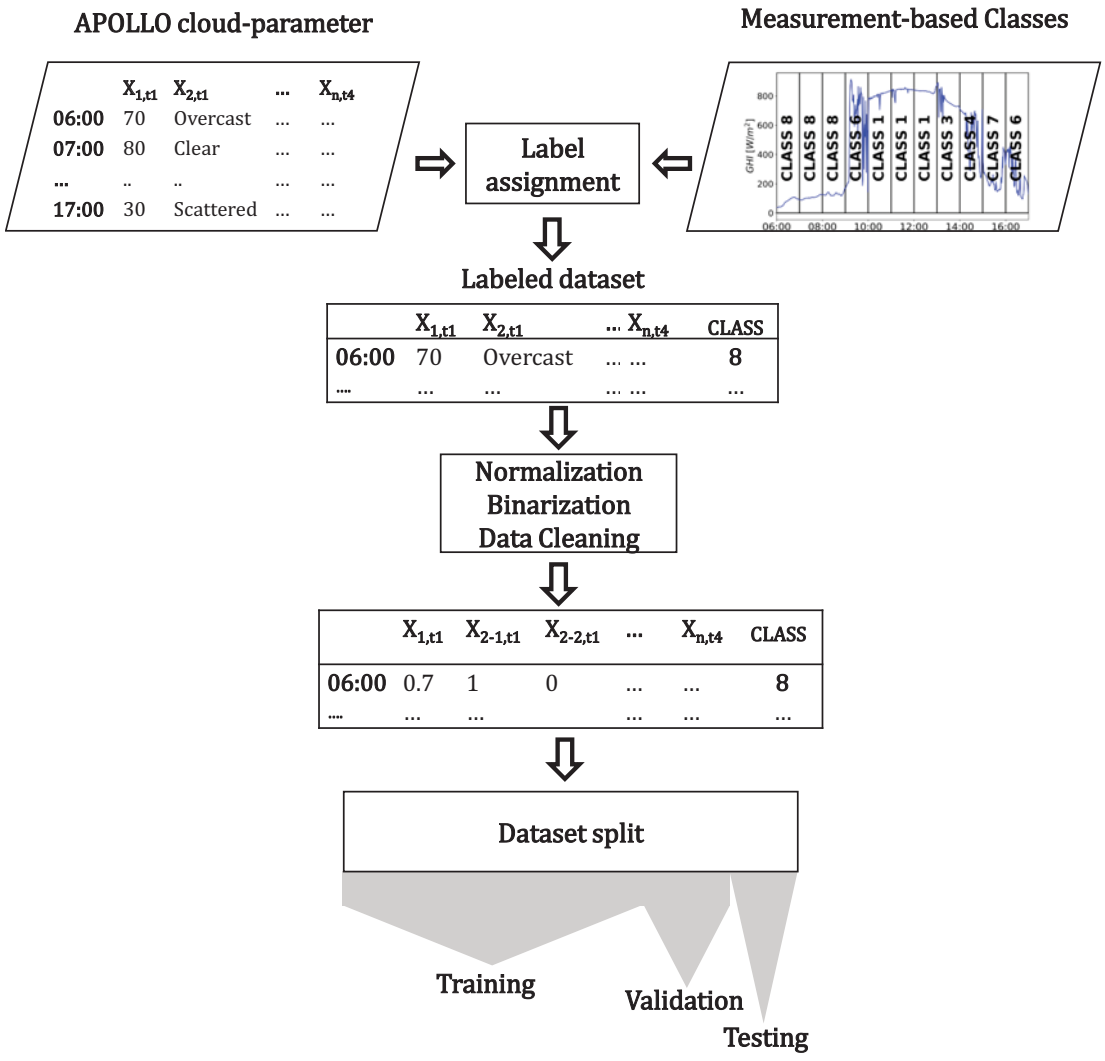

Figure 4: Data preparation process for the training, validation, and testing of the ANN.

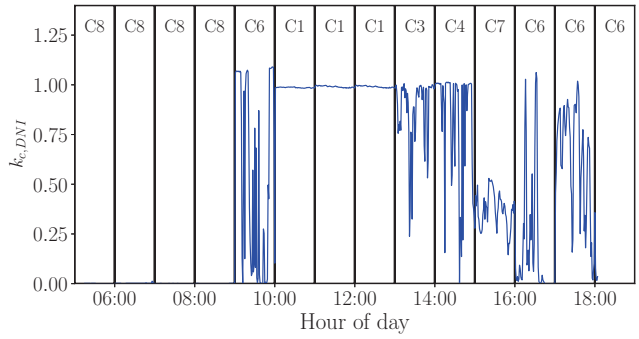

a) 1 min time series of clear-sky index k_c for an example day with different variability classes

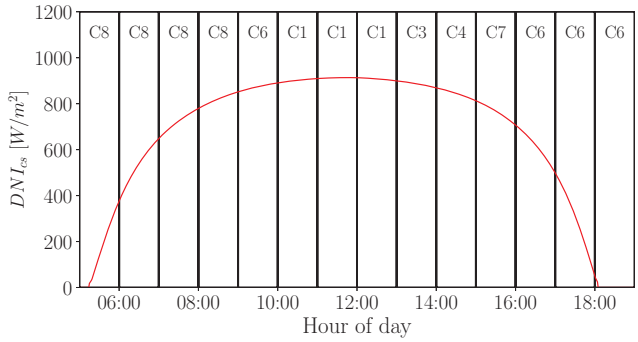

b) Clear-sky DNI for the example day

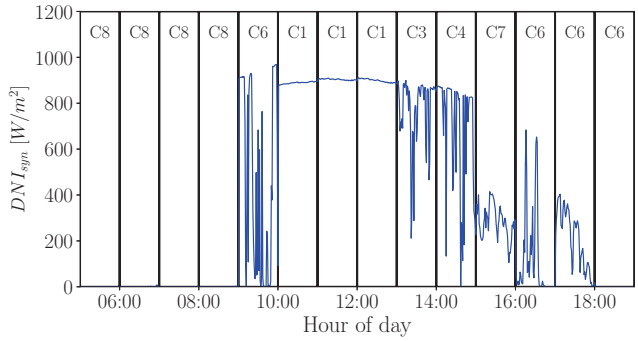

c) Synthetically generated 1 min DNI time series

Figure 5: Time series assembling for the 1 September 2006 at the station of Carpentras as an arbitrarily chosen example. Dimensionless information on the solar radiation variability (a) multiplied by the clear sky radiation estimate of the day (b) results in the synthetic irradiance profile (c).

variability for classes 1 (completely clear) or 8 (completely cloudy), while strongly variable classes 4 and 6 show strong ramps.

As k_c is dimensionless it could be applied to any arbitrary day with a similar temporal sequence of variability classes. In order to take the actual sun position and turbidity state of the cloud-free atmosphere into account, the clear-sky radiation of this day and location (Fig. 5b) is multiplied with the clear-sky index time series.

This results in a synthetic 1 min time series of DNI describing the specific variability situation for a defined day and location (Fig. 5c). As described, the variability classes are randomly drawn from a reference database. They were always classified in fixed, hourly time intervals. Thus, they may include transitions between hours with sudden changes in the variability state as e.g. in the transition between class 6 and class 1 at 10:00 in Fig. 5c. To avoid such unrealistic time series, a smoothing is applied. Reducing the ramp between two irradiation values at time step t to a maximal allowed ramp-rate between a transition of two classes (C_i, C_j). The maximum ramp is defined by the maximum ramp-rate of the two neighboring classes, e.g. $\Delta DNI_{C_i \to C_j,\max}$ for DNI (Annex A1, Table A.2). For the example shown in Fig. 5c this means that maximum ramp-rate of class 6 is obtained from the reference database and the transition between the two classes is limited to a share of that ramp rate and smoothed out over the following time steps. Adapted vales for the new DNI are assigned for the following n timesteps using linear interpolation:

$$DNI_{t+t_n} = DNI_t + t_n \frac{\Delta DNI_{C_i \to C_j}}{n}, \tag{3.2}$$

with

$$n = \left\lceil \frac{\Delta DNI_{C_i \to C_j}}{\Delta DNI_{C_i \to C_j,\max}} \right\rceil, \ \forall t_n \in [1, \ldots, n], \ n \in \mathbb{Z}. \tag{3.3}$$

Parts of the unrealistic ramp rate generated through the model $\Delta DNI_{C_i \to C_j}$ are hereby equally distributed on the following time steps.

4 Results

4.1 Comparing satellite- and ground-based classification

The first objective is to show that the ANN is capable to accurately classify the 1 min irradiance variability only from satellite-based, 15 min resolved cloud textural features. The ANN-based classification results are compared to classifications based on 1 min ground-based observations. Fig. 6 shows the ANN-based classification

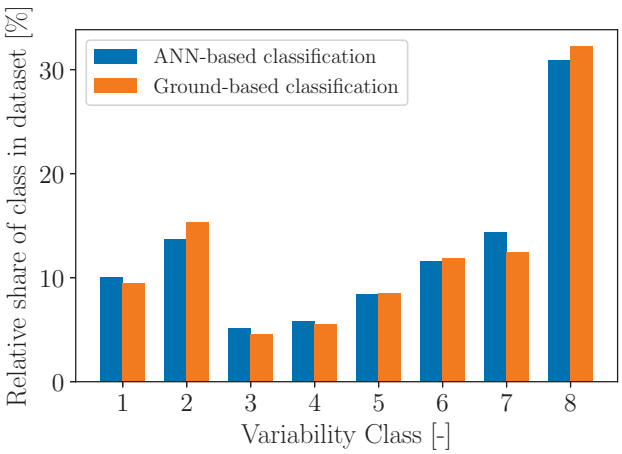

Figure 6: Share of predicted ANN classes vs. ground-based classes for the test dataset (N = 4217).

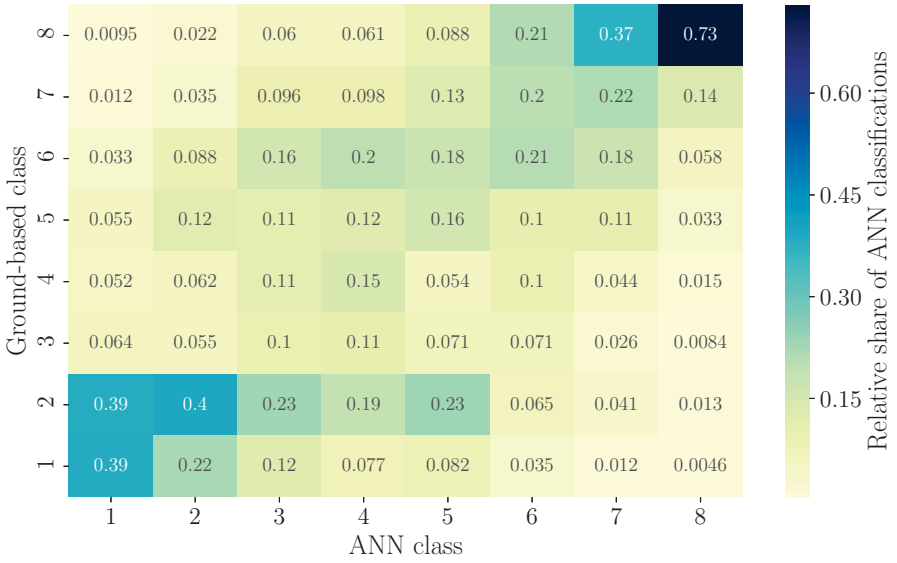

Figure 7: Density heat map as confusion-matrix of the ground-based classification vs. the ANN classification on the validation dataset (N = 4217).

for the whole dataset compared to the classification using ground-based measurements. The optimally trained model results for the test dataset ($N = 4\,217$) in an accuracy to predict the exact same class of 40 %. Since neighboring classes have very similar stochastic characteristic a deviation of ±1 to the next class is acceptable and leads to an accuracy of 69 %. This is slightly better than classification results of Watanabe et al. (2016) applying a satellite-based classification resulting in 56 and 61 % classification accuracy in their data set.

The ground-based classification is used as a benchmark to the new method of ANN-based classification. The figure shows that the distributions of both classifications are alike with small deviations for variability classes 1, 2, 7, and 8. These deviations however are compensated as each of the pairs (1, 2) and (7, 8) consists of one higher and one lower share.

The result in Fig. 6 is produced applying a weighted random choice of the class of the output of the ANN. Choosing the class with highest output probability (*argmax*), leads to more inaccurate results (Figure A.2 in the appendix). This can be explained by the very distinct features of the clear-sky classes (1, 2) and very cloudy classes (7, 8). As the characteristics of the intermediate classes are not very distinguishable the ANN output probabilities for the classes are flat, leading to wrong classifications in favor of clearly distinguishable classes.

The evaluation of the hour by hour classification is shown in the confusion-matrix (Fig. 7). Each cell shows the relative share of a class chosen by the ANN (x-axis) compared to the ground-based classification (y-axis). The confusion-matrix assures the previous observation that classes with distinct features (1, 2, 7, and 8) are correctly classified with only small deviations to neighboring classes (+−1). Intermediate classes however are spread around the diagonal with significant deviations. Still most of classes obtain acceptable results if deviations of ±1 are accepted with an exception for class combination 3–6 and 5–2. This can be explained by the low relative occurrence in the dataset of classes 3 and 5 as well as the strong variability similarity of classes 3 and 6. (Fig. 6)

Overall, the results show that the ANN fails to predict the exact same class for most of the cases. However, the overall distribution of the classes is very similar if the classes are chosen by applying a weighted random choice on the output vector of the ANN (Fig. 6). Therefore, this approach is continued in this study. In a later application the method of deriving the variability class from satellite-based cloud observations in a more classical supervised classification scheme (as discussed in Schroedter-Homscheidt et al., accepted) may replace this neural network approach with a higher accuracy.

4.2 Comparing synthetic and observed irradiance time series

This section demonstrates the results of the application of the method described in Section 3.2. Synthetically generated 1 min time series are benchmarked against ground-based measurements of both DNI and GHI. Fig. 8 shows an example day with almost clear sky conditions and only few small irradiance ramps. This is also represented in the variability classes at the top of the figure dominated by variability class C2 (clear-sky with few clouds). As assumed, the daily cycle of the time-series can be approximated well. Also, the few clouds induce drops in radiation are depicted by the synthetic data (e.g. between 10:00–11:00 for GHI). One can observe that these drops do not necessarily occur in the same hour as in the measured data. Over the whole day however, the number of dips and their magnitude is similar.

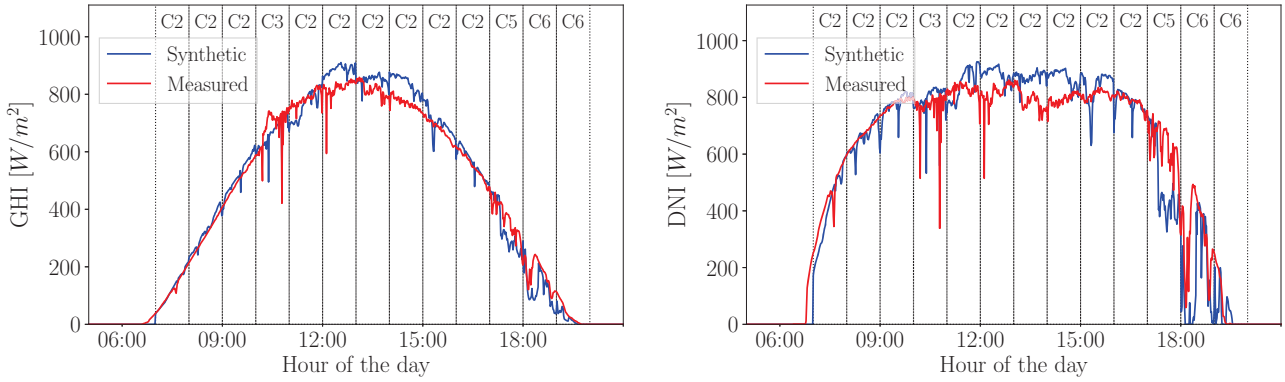

Figure 8: Synthetic and measured GHI (left) and DNI (right) for a clear day at the CENER station (11 April 2010).

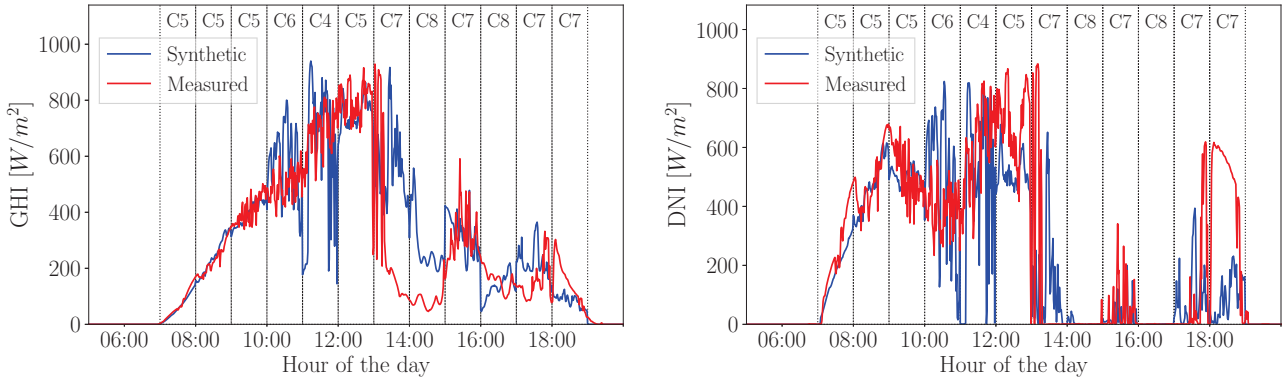

Figure 9: Synthetic and measured GHI and DNI for a cloudy day at the CENER station (29 March 2010).

Fig. 9 shows the same plot for a day with mixed conditions. For the first half of the day high variability in solar irradiance can be observed (Classes 4–6). The second half of the day is dominated by cloudy conditions (C7, C8). The observation described for Fig. 8 is also valid for this day: the strong variability occurring e.g. around 13:00 in the measured data is not reproduced at the same time by the synthetic data as it is a transition process which cannot be exactly described by the variability classes. Instead, similar ramps are occurring shortly before 12:00 in the synthetic data. This observation holds true for the whole day except for the last hour. As no classification was available for this hour due to low sun elevation, the class with the highest probability following the previous class (class 7) was chosen. In this case this is also class 7. However, the actual measurement for this hour suggests an almost clear-sky situation without clouds explaining the difference between synthetic and measured data for the time between 18:00 and 19:00.

Since these example days only provide first insights on the characteristics of the synthetically generated data, the following two figures show results for 3 years at the station CAB. The general correlation between measured and synthetic irradiance is described in the scatter plot in Fig. 10. Hourly averages of the synthetic GHI and DNI are plotted over measured averages. Both figures show strong correlations with a high correlation-coefficient of 0.871 and 0.86 respectively. Only few outliers can be observed especially for DNI. This is explainable by the wrong classification of hours or caused by hours with no existing classification due to data gaps or low sun elevation which were assigned to the most likely class as default. In these cases, outliers are produced similar to the behavior earlier observed at 18:00 in Fig. 9.

Additionally, a small negative bias, i.e. smaller values for the synthetic time series than for the measured time series, can be observed which is more distinct for DNI than for GHI. This is explainable by the used clear-sky radiation model, which tends to a small underestimation of the clear-sky radiation. Also the occurrence of the negative bias in the high DNI value range is an indicator that this originates from the clear-sky model. Therefore, this finding is independent from the cloud induced variability which is the focus of this study. With an expected continuous increase of the model accuracy of the clear-sky model, this error can be reduced.

After this first analysis of the correlation on a timescale of 1 h averages, Fig. 11 shows a comparison of the synthetic and measured 1 min values for the year 2010 at the station CAB. Relative distribution functions are displayed for GHI (left) and DNI (right). Generally, the distribution for GHI can be reproduced by the synthetic data more accurately. However, DNI values

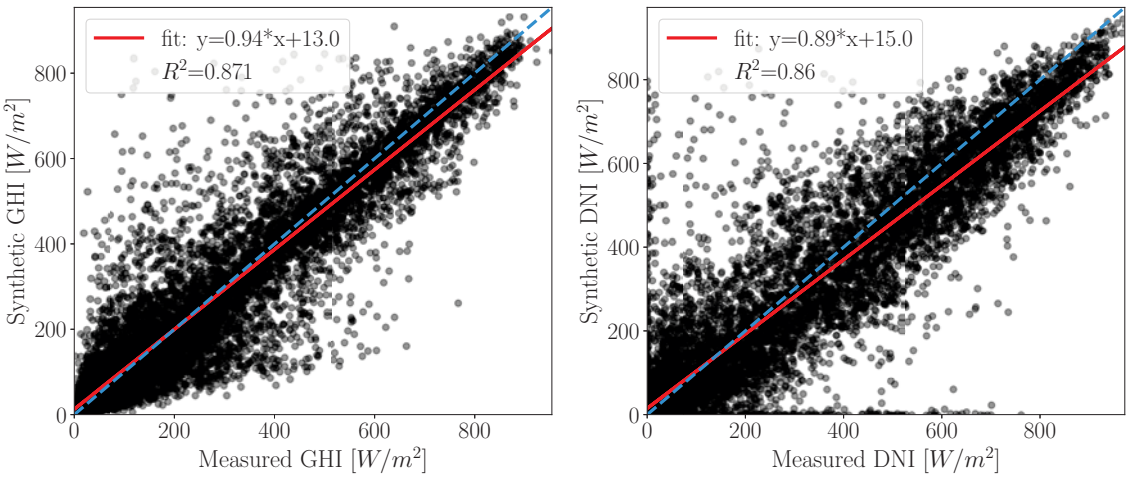

Figure 10: Mean hourly value pairs of measured and synthetic DNI and GHI and the least-squares regression function for the station CAB and the years 2010–2012 (N = 12683).

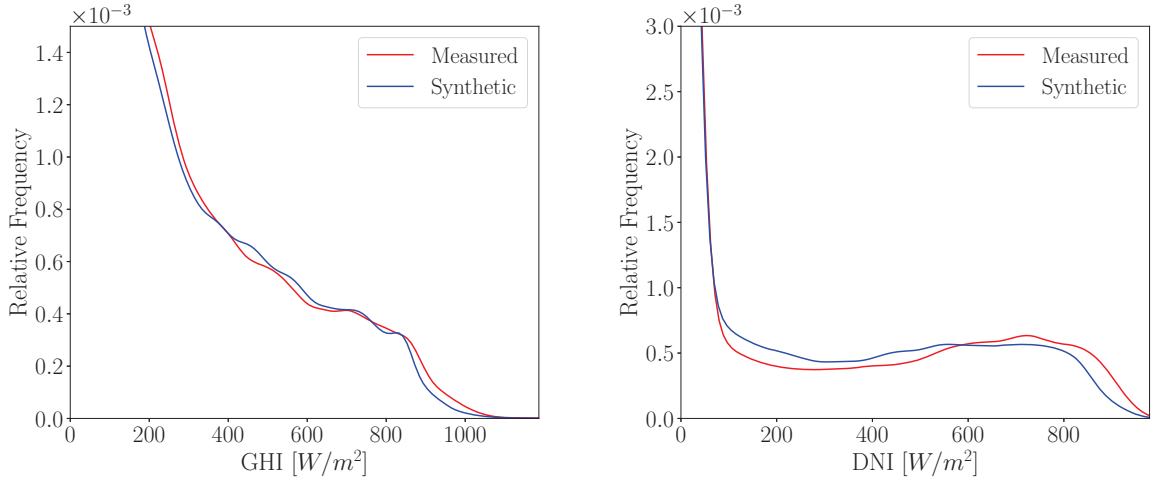

Figure 11: Relative frequency distributions of 1 min DNI and GHI values of synthetic and measured data at CAB for the year 2010.

with lower DNI are over-represented for the synthetic data while the measured data tends to higher DNI values. This can again be explained by the general underestimation of DNI in the clear-sky model.

4.3 Independent data validation

This section presents results for the validation dataset consisting of data from the station Lindenberg for 2016. This is the data subset which has neither been used during the training nor the validation process of the ANN. The classification of variability classes through satellite parameters shows satisfactory results as the distribution of the classes is almost similar to the ground-based classification – the same feature of underestimation of class 2 and 7, and overestimation of class 1 and 8, respectively (Fig. 12).

The relative distribution functions (Figure 13) show a comparable behavior compared to the cases described in Section 4.2 with deviations driven by the clear

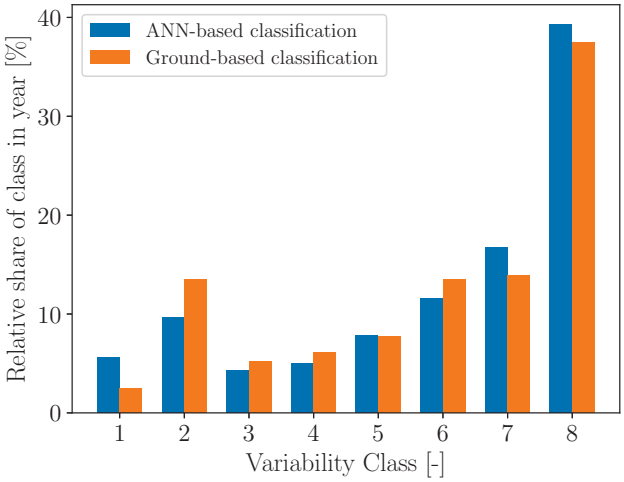

Figure 12: Relative distribution of ANN-based and ground-based classifications for the validation year Lindenberg 2006.

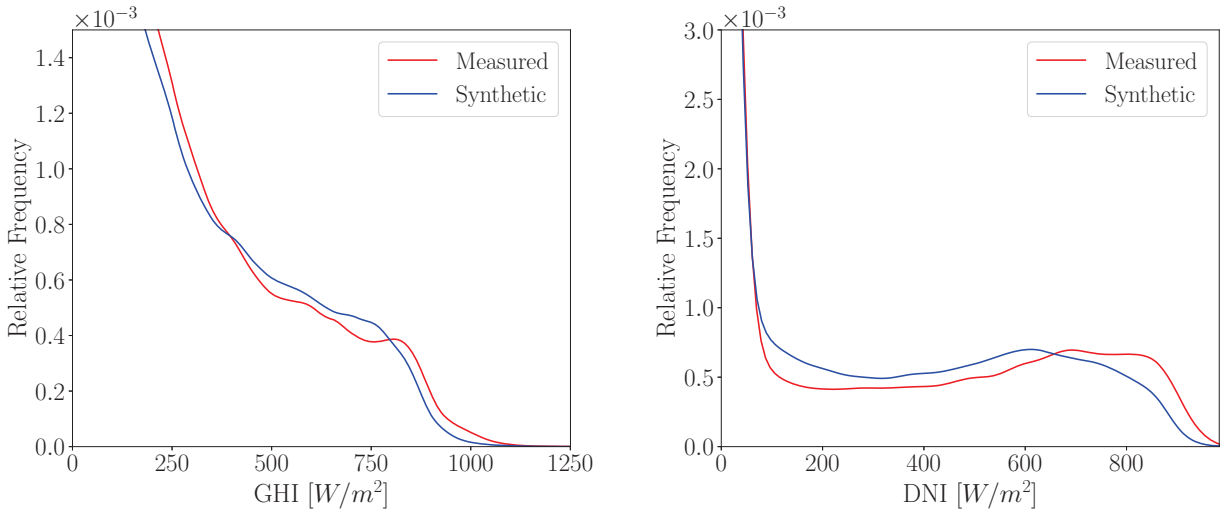

Figure 13: Relative frequency distributions of 1 min synthetic and measured DNI and GHI values for the test data subset at Lindenberg for the year 2006.

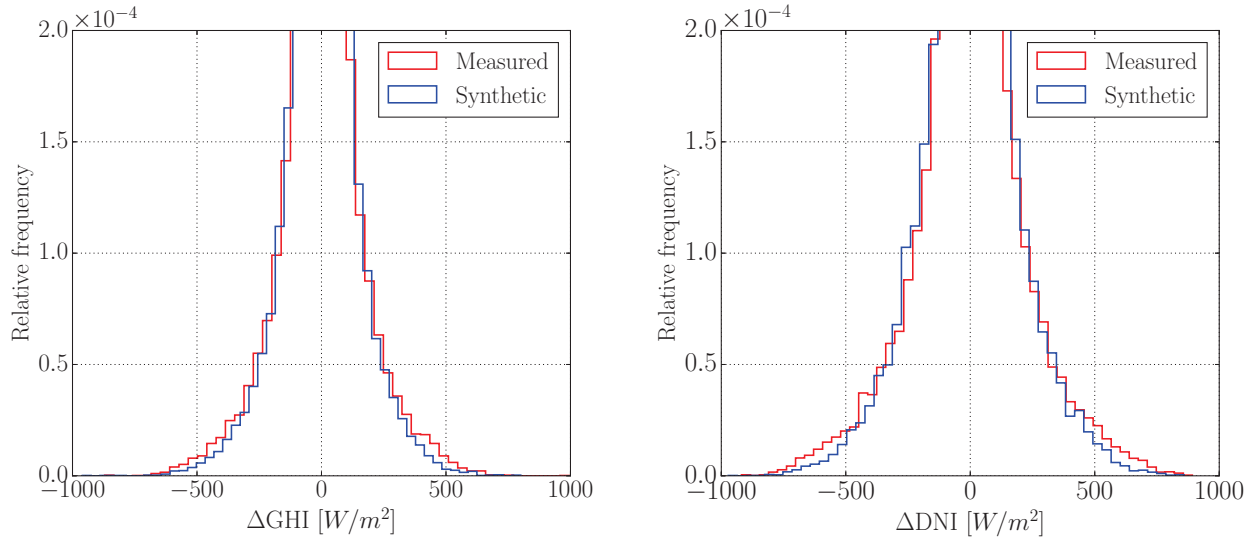

Figure 14: Relative frequency distributions of 1 min GHI and DNI ramp-rates in a histogram with 50 bins for the validation dataset (LIN, 2006).

sky model underestimating the cloud-free situation. A slightly bigger offset between high measured values and synthetic values for both GHI and DNI can be observed. The shapes of both distributions are still alike.

The frequency distribution for ramp-rates (defined as deltas between consecutive 1 min values) in the two datasets are displayed in Fig. 14. In this graph the general underestimation of absolute values is also present. However, the general shape of the ramp-rate distribution is again well represented by the synthetic dataset.

Overall, the validation case on the dataset of Lindenberg for the year 2006 shows that the major differences between synthetic and measured data can be traced back to the general underestimation of clear-sky radiation through the clear sky model. However, the general statistical distribution of ramps is very similar which makes the dataset applicable for modelling of 1 min solar radiation.

4.4 Application case

In order to demonstrate the relevance of 1 min time series, a simplified electrical distribution grid study with high PV shares is conducted. A grid model typical for rural areas as provided by Kerber (2011) is modelled. Load flow calculations are performed using pandapower. (Thurner et al., 2018). The model consists of a one line low-voltage grid with 26 households among which 237 kWp of PV capacity are distributed (Fig. 15). The

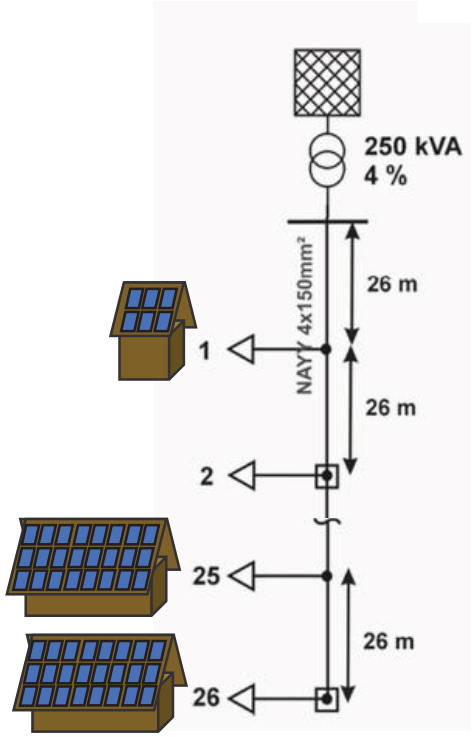

Figure 15: Rural low-voltage distribution grid with high PV Penetration. Adapted from Kerber (2011).

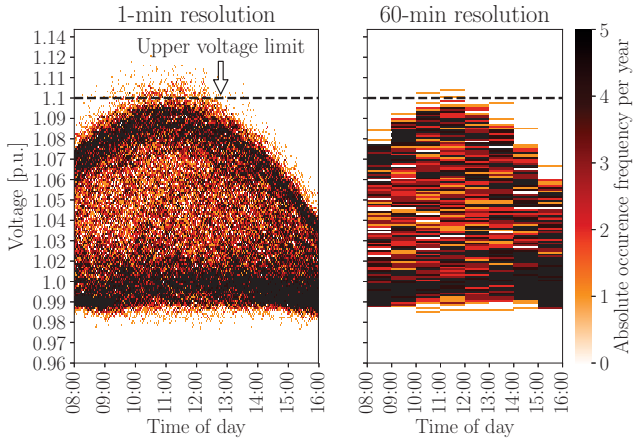

Figure 16: Heatmaps of the voltage at the last PCC (26) of the line in the network from a yearly calculation using synthetic 1 min time series for the station of Lindenberg.

simulations are performed with the generated 1 min synthetic solar irradiance data for the validation site Lindenberg and household load profiles from Tjaden et al. (2015).

A typical concern for distribution system operators is that with increasing PV feed-in the voltage rises above a certain limit defined by grid codes as e.g. DIN EN 50160. This happens especially during times of low demand and high PV feed-in in weak, unmeshed grids such as the example grid described above. Fig. 16 shows the voltage at the end of the point of common coupling (PCC) at the end of the line for a yearly simulation with 1 min values (left) and hourly means (right). It is clearly depictable that a neglection of sub-hourly solar irradiance variability leads to less critical voltage values, i.e. above 1.1 per unit (p.u.) increase. Over the whole year, 1890 voltage violations occur in the 1 min simulation. Only 7 hours (representing 420 minutes) are affected by voltage violations for the 1 h simulation. If the same simulation is performed using the actual measurement data for Lindenberg in 2006 instead of the generated synthetic data a total sum of 2008 violations occur.

In contrast to the higher deviations for synthetic over measured data discussed in Section 4.2 (mainly for DNI) the deviations between synthetic and observed data impacts are much smaller. This application illustrates that from the user's point of view the accurate representation of ramp rates and irradiance value distributions are of large importance while the actual agreement in each minute of irradiance values is of less importance for the quantification of electrical grid behavior.

5 Conclusions

Solar irradiation in the temporal domain of 1 min is relevant for researchers, electrical grid operators, and solar energy project developers. As this type of data is only sparsely available through ground-based measurements, a method to generate this data for arbitrary locations is valuable. The 1 min variability is mainly caused by heterogeneous slowly passing clouds as e.g. cirrus or stratus clouds or by quickly passing cumulus-like clouds.

In this paper, such a method is developed using an ANN to classify irradiance variability using only parameters derived from geostationary satellites observing cloud fields. Such satellite observations are available for Europe, Africa, and the Middle East since 2004 and will be available in future on a global scale. The ANN is trained and tested using 3 stations from the BSRN surface radiation network and an automated classification of variability as observed by ground observations. The results show that the ANN is able to reproduce the statistical distribution of variability classes over the test dataset with acceptable accuracies compared to other studies.

Furthermore, this study suggests a method to convert the variability classes into a time series with 1 min resolution for DNI and GHI. This is done by super-imposing a randomly chosen information of kc variability to a clear-sky model. This information is derived from the respective variability class out of an existing reference data base. The comparison of such synthetically generated values to actual ground-based measurements show that the overall distribution of 1 min absolute values and ramps can be reproduced by the model. However, a general negative bias of the model towards higher values of DNI can be observed. This can be traced back to an underestimation in the cloud-free situations by the clear sky model representing aerosols and water vapor based atmospheric turbidity.

An application of such synthetically generated data to a low-voltage electrical grid study highlights the relevance of 1 min resolved input data. A large underestimation of critical voltage band violations using hourly means instead of 1 min data can be observed. With the synthetically generated data as proposed in this paper, the 1 min violations are only slightly under-estimated compared to results derived from ground observations of irradiances.

Two main aspects can be considered for a future improvement of the model: Future improvements of clear-sky models can further enhance the accuracy of the approach. This might resolve the general negative bias as observed in the results section. Furthermore, additional training data from other years and at more stations as well as further tuning of the ANN hyperparameters might lead to an improvement of the classification performance. Especially classes which are underrepresented in the current dataset, i.e. classes with strong variability (Class 3–6) can increase the performance of the classification of indistinctive classes.

Acknowledgements

The authors would like to thank the personnel from the Baseline Surface Radiation Network (BSRN) stations at Cabauw, Carpentras, CENER, and Lindenberg for all observations.

A1 Variability classes

The reference database containing individual time series for each variability class is defined in detail in Schroedter-Homscheidt et al. (2018 and accepted). This includes GHI and DNI related variability indices, ramp rate statistics, and a graphical visualization of the database itself.

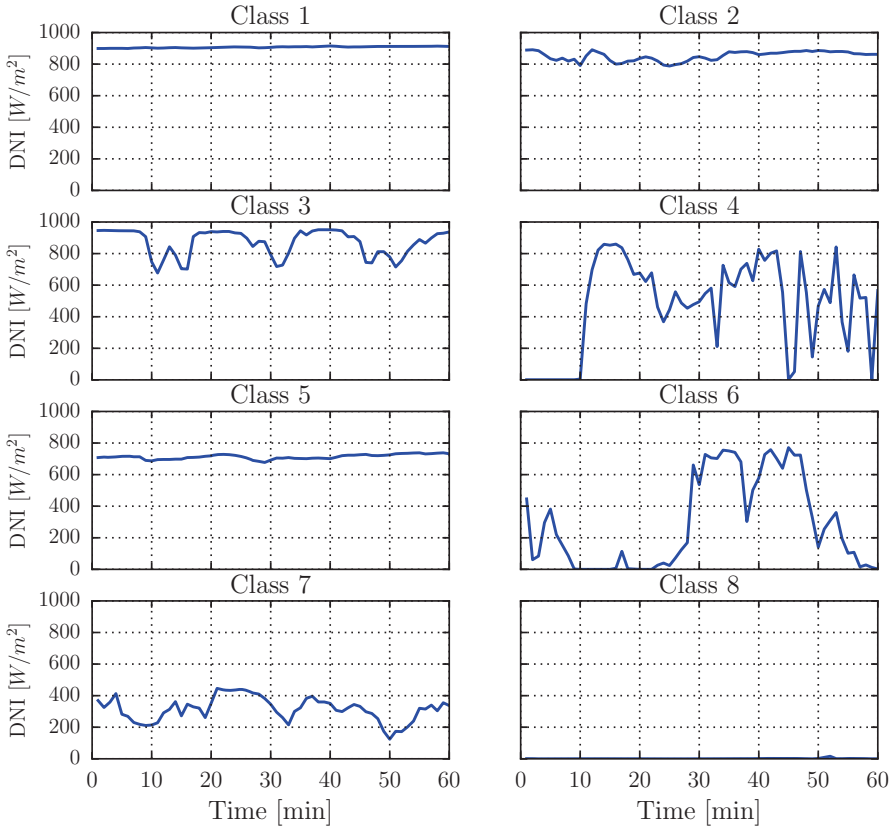

Figure A.1: Samples of DNI for each variability class from the reference database (Schroedter-Homscheidt et al., 2018)

Table A.1: Variability class characterization by k_c DNI, the number of direction changes in DNI within the hour (CSFD), and the number of cases in the reference database. All median values and the P25 and P75 range (in brackets) are given as provided in SCHROEDTER-HOMSCHEIDT et al. (2018).

class	short description	median k_{cDNI} [-]	CSFD in DNI [-]	#
1	very high DNI, low CSFD	0.99 (0.98, 1.04)	0 (0, 0)	63
2	high DNI, low CSFD	0.96 (0.93, 1.04)	0 (0, 2)	36
3	high DNI, medium CSFD	0.93 (0.91, 0.95)	8 (5, 12)	25
4	high DNI, medium CSFD	0.79 (0.75, 0.87)	16 (10, 17)	16
5	medium DNI, small CSFD	0.75 (0.68, 0.82)	3 (0, 6)	39
6	medium DNI, high CSFD	0.48 (0.35, 0.63)	15 (12, 19)	51
7	low DNI, medium CSFD	0.18 (0.12, 0.25)	7 (5, 9)	44
8	low DNI, low CSFD	0.00 (0.00, 0.01)	0 (0, 0)	38

A2 Cloud parameters used as input for the ANN

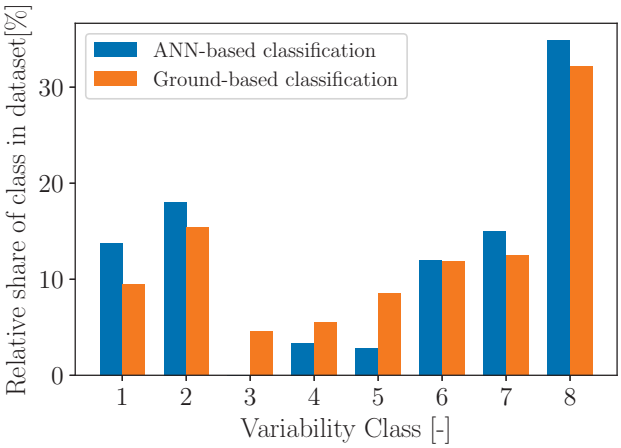

Figure A.2: Share of predicted ANN classes vs. ground-based classes for the test dataset (N = 4217) applying the argmax function on the output layer.

Table A.2: Variability class characterization by ramp rates of DNI. All median values and the P25 and P75 range (in brackets) are given as provided in SCHROEDTER-HOMSCHEIDT et al. (2018).

Class	ΔDNI_{mean} [W/m^2]	ΔDNI_{σ} [W/m^2]	ΔDNI_{max} [W/m^2]
1	1.2 (0.8, 1.4)	1 (0.8, 1.2)	4 (3, 5)
2	11.5 (5.6, 14.5)	13.3 (6.8, 21.8)	62 (36, 96)
3	51.9 (30.6, 82.6)	96.8 (49.6, 118.2)	414 (257, 483)
4	130.3 (108.0, 168.2)	187.2 (139.4, 216.1)	730 (542, 774)
5	23.3 (14.3, 40.0)	22.9 (12.8, 40.4)	109 (55, 185)
6	118.1 (91.2, 155.0)	143.4 (112.5, 173.8)	569 (477, 674)
7	49.3 (34.4, 58.7)	57.0 (37.4, 69.2)	238 (171, 323)
8	0.3 (0.1, 1.8)	0.8 (0.3, 4.2)	4 (1, 17)

A3 Variability class classification using argmaxs

Table A.3: List of parameter descriptions of cloud parameters used during training.

Parameter ID	Description
0	Cloud coverage in pixel (%)
1	Cloud fraction in window (%)
2	Mean cloud coverage in window (%)
3	1σ variability of coverage in window (%)
4	Number of cloud→cloud-free changes among pixels in window ([–])
5	Relative number of cloud→cloud-free changes among pixels in window (%)
6	Number of clouds in window
7	Fractal Box Dimension (FBD) ([–])
8	r of FBD linear fit ([–])
9	Cloud mask type: Cloud (binary)
10	Cloud mask type: Clear land (binary)
11	Cloud mask type: Snow/Ice (binary)
12	Cloud area type: Scattered (binary)
13	Cloud area type: Broken overcast (binary)
14	Cloud area type: Thin ice (binary)
15	Cloud area type: Clear (binary)
16	Cloud type/height: Low (binary)
17	Cloud type/height: Medium (binary)
18	Cloud type/height: High (binary)
19	Cloud type/height: Thin ice (binary)
20	Time of day (minute of day/1440)

References

Carvalho, L.M.V., M.A.F. Silva Dias, 1998: An Application of Fractal Box Dimension to the Recognition of Mesoscale Cloud Patterns in Infrared Satellite Images. – Appl. Meteor. **37**, 1265–1282, DOI:10.1175/1520-0450(1998)037<1265:AAOFBD>2.0.CO;2.

Deane, J.P., G. Drayton, B.P. Gallachir, 2014: The impact of sub-hourly modelling in power systems with significant levels of renewable generation. – Appl. Energy. **11**. 152–158. DOI: 10.1016/j.apenergy.2013.07.027.

Fernández-Peruchena, C.M., M. Gastón, 2016: A simple and efficient procedure for increasing the temporal resolution of global horizontal solar irradiance series. – Renew. Energy **86**, 375–383. DOI:10.1016/j.renene.2015.08.004.

Gschwind, B., L. Wald, P. Blanc, M. Lefèvre, M. Schroedter-Homscheidt, A. Arola, 2019: Improving the McClear model estimating the downwelling solar radiation at ground level in cloud-free conditions – McClear-v3. – Meteorol. Z. **28**, 147–163. DOI : 10.1127/metz/2019/0946.

Grantham, A.P., P.J. Pudney, L.A. Ward, M. Belusko, J.W. Boland, 2017 **:** Generating synthetic five-minute solar irradiance values from hourly observations. – Sol. Energy **147**, 209–221. DOI:10.1016/j.solener.2017.03.026.

Jung, S., 2015: Variabilität der solaren Einstrahlung in 1-Minuten aufgelösten Strahlungszeitserien. – Master thesis, Universität Augsburg, Germany.

Jamaly, M., J.L. Bosch, J. Kleissl, 2013: Aggregate Ramp Rates of Distributed Photovoltaic Systems in San Diego County. – IEEE Transactions on Sustainable Energy 4, 2, 519–526. DOI:10.1109/TSTE.2012.2201966.

Kerber, G., 2011: Capacity of Low Voltage Distribution Networks Due to Power generation of Small Photovoltaic Power Plants. – Ph.D. dissertation, Technical University of Munich.

Kriebel, K.T., R.W. Saunders, G. Gesell, 1989: Optical Properties of Clouds Derived from Fully Cloudy AVHRR Pixels. – Beitr. Phys. Atmos. **62**, 165–171. DOI: elib.dlr.de:64671.

Kriebel, K.T., G. Gesell, M. Kästner, H. Mannstein, 2003: The cloud analysis tool APOLLO: Improvements and Validation. – Int. J. Rem. Sens. **24**, 2389–2408. DOI:10.1080/01431160210163065.

Lave, M., J. Kleissl, 2010: Solar variability of four sites across the state of Colorado. – Renew. Energy **35**, 2867–2873. DOI: 10.1016/j.renene.2010.05.013.

Lave, M., M.J. Reno, R.J. Broderick, 2015: Characterizing local high-frequency solar variability and its impact to distribution studies. – Solar Energy **118**, 327–337.

Lefévre, M., A. Oumbe, P. Blanc, B. Espinar, B. Gschwind, Z. Qu, L. Wald, M. Schroedter-Homscheidt, C. Hoyer-Klick, A. Arola, B. Benedetti, J.W. Kaiser, J.-J. Morcrette, 2013: McClear: A new model estimating downwelling solar radiation at ground level in clear-sky conditions. – Atmos. Meas. Tech. **6**, 2403–2418, DOI:10.5194/amt-6-2403-2013.

Li, S., M. Hongjie, W. Li, 2017: Typical solar radiation year construction using k-means clustering and discrete-time Markov chain. – Appl. Energy **205**, 720–731. DOI:10.1016/j.apenergy.2017.08.067.

Lingfors, D., 2015: Solar Variability Assessment and Grid Integration – Methodology Development and Case Studies. – Ph.D. dissertation, Uppsala University. DOI: DiVA.org:uu-265451.

Nouri, B., S. Wilbert, P. Kuhn, N. Hanrieder, M. Schroedter-Homscheidt, A. Kazantzidis, L. Zarzalejo, P. Blanc, S. Kumar, N. Goswami, R. Shankar, R. Affolter, R. Pitz-Paal, 2019: Real-Time Uncertainty Specification of All Sky Imager Derived Irradiance Nowcasts. – Remote Sens. **11**. DOI:10.3390/rs11091059.

Ohmura, A., E.G. Dutton, B. Forgan, C. Fröhlich, H. Gilgen, H. Hegner, A. Heimo, G. König-Langlo, B. Mcarthur, G. Müller, R. Philipona, C.H. Pinker, K. Whitlock, K. Dehne, 1998: Baseline Surface Radiation Network (BSRN/WCRP): New Precision Radiometry for Climate Research. – Bull. Amer. Meteor. Soc. **79**, 2115–2136. DOI:10.1175/15200477(1998)079<2115:BSRNBW>2.0.CO;2.

Perez, R., S. Kivalo, J. Schlemmer, K. Hemker, T.E. Hoff, 2012: Short-term irradiance variability: Preliminary estimation of station pair correlation as a function of distance. – Sol. Energy **86**, 2170–2176, DOI:10.1016/j.solener.2012.02.027.

Perez, R. , Richard, M. David., T. Hoff, M. Jamaly, S. Kivalo, J. Kleissl, P. Laure, M. Perez, 2016: Spatial and Temporal Variability of Solar Energy. – Foundations and Trends in Renewable Energy **1**, 1–44, DOI:10.1561/2700000006.

Saunders, R.W., K.T. Kriebel, 1988: An improved method for detecting clear sky and cloudy radiances from AVHRR data. – Int. J. Rem. Sens. **9**, 123–150, DOI:10.1080/01431168808954841.

Sengupta, M., A. Habte, S. Kurtz, A. Dobos, S. Wilbert, E. Lorenz, T. Stoffel, D. Renné, C. Gueymard, D. Myers, S. Wilcox, P. Blanc, R. Perez, 2015: Best Practices Handbook for the Collection and User of Solar Resource Data for Solar Energy Applications. – Technical report NREL/TP-5D00-63112 in collaboration with International Energy Agency Solar Heating and Cooling Programme Task 36 and 46.

Scholz, J. , 2012: Renewable energy based electricity supply at low costs: development of the REMix model and application for Europe. – Ph.D. dissertation, University of Stuttgart.

Schreck, S. , 2018: Implications of Sub-Hourly Solar Radiation Variability on Decentralized Energy Systems- Generation of Synthetic Time Series and Model-Based Assessment. – Master thesis, University of Stuttgart, Germany.

Schroedter-Homscheidt, M., S. Jung, M. Kosmale, 2018: Classifying ground-measured 1 minute temporal variability within hourly intervals for direct normal irradiances. – Meteorol. Z. **27**, 2, 160–179. DOI:10.1127/metz/2018/0875.

Schroedter-Homscheidt, M., M. Kosmale, Y.-M. Saint-Drenan, accepted: Classifying direct normal irradiance 1 minute temporal variability from 15 min resolved geostationary satellite-based cloud observations. – Meteorol. Z., accepted.

Thurner, L., A. Schneidler, F. Schaefer, J.H. Menke, J. Dollichon, F. Meier, S. Meinecke, M. Braun, 2017: Pandapower – an Open Source Python Tool for Convenient Modeling, Analysis and Optimization of Electric Power Systems. DOI:10.1109/TPWRS.2018.2829021.

Tjaden, T., J. Bergner, J. Weniger, V. Quaschning, 2015: Repräsentative elektrische Lastprofile für Wohngebäude in Deutschland auf 1-sekündiger Datenbasis. DOI:10.13140/RG.2.1.5112.0080.

Watanabe, T., Y. Oishi, T.Y. Nakajima, 2016: Characterization of surface solar-irradiance variability using cloud properties based on satellite observations. – Sol. Energy **140**, 83–92. DOI:10.1016/j.solener.2016.10.049.

Wey, E., M. Schroedter-Homscheidt, 2014: APOLLO Cloud Product Statistics. – Proc. SolarPACES 2013 Conference in Energy Procedia **49**, 2414–2421, DOI:10.1016/j.egypro.2014.03.256.

Wiemken, E., H.G. Beyer, W. Heydenreich, K. Kiefer, 2001: Power characteristics of PV ensembles: experiences from the combined power production of 100 grid connected PV systems distributed over the area of Germany. – Sol. Energy **70**, 513–518, DOI:10.1016/S0038-092X(00)00146-8.

Wolf, P., J. Vèelák, 2018: Simulation of a simple PV system for local energy usage considering the time resolution of input data. – J. Energy Storage **15**, 1–7. DOI:10.1016/j.est.2017.10.009.

Zhang, G.P. , 2000: Neural networks for classification: a survey. – IEEE Transactions on Systems, Man, and Cybernetics **30**, 451–462. DOI:10.1109/5326.897072.